Stacking- and chirality-dependent collapse of single-walled carbon nanotubes: A large-scale density-functional study

A. Impellizzeri,[1] P. Briddon,[2] and C. P. Ewels[1,*]

[1]*Institut des Matériaux Jean Rouxel (IMN), UMR 6502, CNRS, Université de Nantes, 2 rue de la Houssinière, 44322 Nantes Cedex 3, France*

[2]*Department of Electrical Engineering, Newcastle University, Newcastle-Upon-Tyne NE1 7RU, United Kingdom*

(Received 8 April 2019; revised manuscript received 23 July 2019; published 9 September 2019)

Using density functional theory with van der Waals (vdW) corrections, we study the collapse of free-standing single-walled carbon nanotubes (also called "dogbone" nanotubes). Their thermodynamic stability is strongly influenced by the initial stacking sequence, with lateral shear allowing registry change with turbostratic stacking predominant. The electronic structure of collapsed zigzag and armchair carbon nanotubes is investigated, demonstrating sensitivity to the lattice registry. The opening of small (meV) band gaps is shown for both armchair and zigzag collapsed nanotubes, arising from quantum confinement and charge transfer between the bilayer graphenelike central region and nanotubelike edges. Different scaling rules for the band gaps of collapsed carbon nanotubes are obtained as a function of their widths taking stacking and chirality into account. We reconcile a complete understanding of electronic properties in these deformed tubes with literature theoretical and experimental results, suggesting collapsed nanotubes can be promising candidates as conductive nanoribbons in electronic and spintronic device applications.

DOI: 10.1103/PhysRevB.100.115410

I. INTRODUCTION

Soon after the seminal single-walled carbon nanotube (SWCNT) publication by Iijima *et al.* [1], it was realized that above a certain diameter such tubes are not stable. Instead, they spontaneously collapse [2], with cross section composed of two edge "bulbs" (resembling small radius circular CNTs), connected by a flat region in the middle similar to bilayer graphene. Such collapsed tubes are also referred to in the literature as "dogbone nanotubes," and "fully flattened carbon nanotubes." The thermodynamic driving force for collapse is given by a trade-off between the interlayer attractive interaction (E_{vdW}) in the central graphenelike zone [3,4] against the additional repulsive strain (E_{strain}) caused by localizing the curvature at each edge zone [5,6], as follows: $\Delta E_{\mathrm{eq}} = W_{\mathrm{flat}}E_{\mathrm{vdW}} - 2E_{\mathrm{strain}}$ (see Fig. 1). Since the central surface energy interaction is width dependent, the structural transition from circular to collapsed is a function of nanotube diameter [7], and happens spontaneously above a given threshold D_{cross}. Collapsed nanotubes are structurally defined by two parameters, namely the chiral vector of the original uncollapsed tube, and also an interlayer shear which is introduced due to the symmetry lowering and can change the interlayer registry.

Various experimental approaches result in large diameter CNTs, including multiwalled carbon nanotube unzipping (for example by acid treatment, intercalation, and exfoliation with heating, electrical current, and high-vacuum nanomanipulation) [8], sonication after thermal oxidation [9,10], arc discharge [2,11], laser vaporization [12], and chemical vapor deposition (CVD) [13–17]. Tube collapse can also occur due to external factors such as pressure [18], temperature [19], electron beam irradiation [20–23], and bundling [24–27].

TEM studies suggest that for freestanding SWCNTs the threshold diameter for collapse D_{cross} is 5.1 nm [17] and 4.6 nm when in bundles [28], and is largely independent of nanotube chirality [13]. Before the thermodynamic collapse threshold diameter (D_{cross}) a smaller threshold diameter (D_{meta}) is seen in the models, above which a collapsed configuration is metastable but thermodynamically unfavorable compared to a circular tube [17]. Computational modeling, mostly using molecular dynamics (MD), molecular mechanics, and continuum elasticity, gives the metastable diameter D_{meta} from 1.4–2.7 nm. However calculated D_{cross} values show large variation with calculated values from 2.0–8.8 nm [5,7,16,17,29–39].

Stacking order is not controllable in collapsed tubes, and the role of lattice registry in tube collapse remains unclear [40]. The electronic properties of AB- and AA-stacked armchair collapsed nanotubes have been compared with that of hydrogen-edge terminated zigzag bilayer GNRs [38]. Both show the opening of a small band gap compared to infinite bilayer graphene, whose origin has not been fully explored. More generally, AB and AA represent extreme stacking limits, and intermediate stacking closer to the chiral nanotubes in experiment have not been studied. Previous studies have shown the differences in electronic structure (metallic and semiconductor) between armchair and zigzag chirality in both mono- and bilayer GNRs and circular carbon nanotubes. Similarly it is important to consider the electronic structure of collapsed zigzag nanotubes, which has not been reported to date.

In the present paper we make a detailed *first-principle* investigation of the radial deformation and consequent collapse of SWCNTs, employing several DFT approximations

*Corresponding author: chris.ewels@cnrs-imn.fr

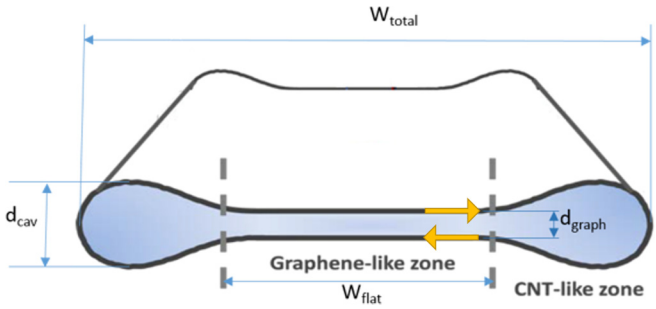

FIG. 1. Schematic representation of collapsed single-walled carbon nanotube. Labels indicate terms used throughout the paper, W_{total} = width of collapsed nanotube, W_{flat} = width of flat bilayer graphenelike central section, d_{graph} = interlayer spacing of central section, d_{cav} = diameter of edge cavities. Orange arrows show interlayer shear mode.

and relativistic Gaussian basis sets. We determine at what diameter SWCNTs stably collapse, taking the effects of layer registry and tube chiralities into account. The electronic structures of collapsed nanotubes are analyzed unraveling the key role of the edge cavities, along with a full exploration of the band gap emergence and its sensitivity to the stacking sequence and shaped edges (armchair and zigzag). Band gaps for the different types of nanotubes of homogenous stacking vary. Such a study provides detailed understanding of the impact of translational and rotational rolling can have on the self-collapsing of free-standing SWCNTs and their electronic properties. This work constitutes a solid benchmark for the on-going development of an atomistic model for the qualitative aspects of potential applications in optoelectronics [41], nanoelectronics [42], and spintronics [43].

II. COMPUTATIONAL METHODS

The current study draws on density functional theory (DFT) and compares with classical adaptive intermolecular reactive empirical bond order (AIREBO) force fields [44]. For AIREBO computations we used the large-scale atomic/molecular massively parallel simulator (LAMMPS) package [45]. The AIREBO potential is composed of a reactive empirical bond order (REBO) term for short-range interactions, a Lennard-Jones term defining long-range vdW interactions, and a torsional term describing dihedral angle preferences. A model system of 12 unit cells was used to simulate circular/collapsed carbon nanotubes with different diameters/widths containing 400–1520 atoms. Both unit cell and atom coordinates were fully optimized until the force on each atom is smaller than 10^{-9} eV/Å and total energy converged to a very high tolerance of 10^{-14} eV. Energy minimization was carried out applying an external pressure tensor to the box along the periodic nanotube axial direction.

All DFT calculations are performed with the AIMPRO code [46–48]. We used the local density approximation (LDA) and generalized gradient approximation (GGA) parametrized by Perdew, Burke, and Ernzerhof (PBE) [49]. To describe the interlayer interaction between the upper and lower layer in the central region three versions of Grimme's dispersion corrections were tested: D1 [50], D2 [51], and D3 [52] with Becke-Johnson (BJ) damping [53]. Relativistic pseudopotentials are included via the Hartwigsen-Goedecker-Hütter scheme [54]. The wave function basis consists of Gaussian function sets multiplied by polynomial functions including all angular momenta up to maxima $p(l = 0 - 1)$, $d(l = 0 - 2)$, and $f(l = 0 - 3)$ [55]. In order to test the importance of basis set convergence, two carbon basis sets *pdpp* and *pdddp* were tried, giving 22 and 38 independent functions per atom, respectively. Hydrogen was treated using a *ppp* basis set with 12 independent functions. A system-dependent plane-wave energy cutoff of 175 Ha (Ha: Hartree energy) was taken, and a nonzero electron temperature of $kT = 0.04$ eV for electronic level occupation using a Fermi smearing function.

Hexagonal and orthorhombic unit cells are used to contain circular and collapsed nanotubes, respectively, with periodic boundary conditions applied. Sufficient space between neighboring species (>20.0 Å) in the radial direction is set to avoid interaction.

Brillouin zone sampling was made with Monkhorst-Pack (MP) method with dense k-point meshes ($1 \times 24 \times 1$ and $1 \times 16 \times 1$ grids for armchair and zigzag collapsed nanotubes respectively, with a $1 \times 240 \times 1$ extrapolated grid used for self-consistent electronic structure calculations) with origin at Γ. Nanotube geometry and axial unit cell length are simultaneously optimized with no constraints, until the maximum atomic position change in a given iteration drops below $10^{-7}\, a_0$ (a_0: Bohr radius) and total energy is converged to within a tolerance of 10^{-7} Ha. Reaction barriers are calculated using the climbing nudged elastic band model [56]. The charge transfer process from curved edges and central flat region are determined by Mulliken [57] and Bader [58] analysis. To distinguish the local interaction between graphene layers, different stackings are considered.

III. RESULTS AND DISCUSSION

In general, the stacking in collapsed tubes will be turbostratic. There are some cases where "exceptional" stacking can be seen, the main example is armchair nanotubes where with appropriate shearing it possible to generate central zones in AA stacking, AB stacking, or translational intermediates. In bilayer graphene AA behaves like turbostratic stacked (decoupled) material, whereas stronger coupling in AB significantly alters the band structure [59]. Therefore, in the armchair nanotube studies, we have generated collapsed tubes with AA, AB, and intermediate interlayer stackings, and the zigzag collapsed tubes with AB′ stacking.

A. Geometry of collapsed armchair SWCNTs

We consider here a range of different diameter armchair (n, n) nanotubes. The total energy difference between flattened ($E_{\text{tot}}^{\text{collapsed}}$) and cylindrical ($E_{\text{tot}}^{\text{circular}}$) tubes is compared to determine the threshold diameter above which collapsed tubes are the most stable configuration. Both this crossing point and the optimized geometries of the collapsed tubes are quite dependent on the level of theory used, notably the interlayer distance in the central bilayer section and the cavity height at the edges (see Fig. 1 and Table I).

AIREBO underestimates the collapse threshold diameter and cavity size (consistent with literature [16,17,60,61]),

TABLE I. Calculated geometry parameters and metastable (D_{meta}) and threshold (D_{cross}) diameters (nm) between cylindrical and collapsed carbon nanotubes with different theoretical approaches (AIREBO empirical potential, DFT using LDA, GGA-PBE, and GGA-PBE with Grimme dispersion corrections).

Collapsing armchair (*n*,*n*) tubes					
Method	Interlayer stacking	Central interlayer distance d_{graph} (nm)	Edge cavity height d_{cav} (nm)	Metastable collapse threshold diameter D_{meta} (nm)	Stable collapse threshold diameter D_{cross} (nm)
AIREBO	AA	0.341	0.706	1.800	4.075
	AB	0.340	0.701	1.800	4.075
LDA	AA	0.350	0.895	2.987	7.787
	AB	0.333	0.878	2.987	7.256
PBE	AA	0.450	1.078	3.497	–
	AB	0.441	1.060	3.497	–
PBE-D1	AA	0.349	0.812	1.904	5.699
	AB	0.324	0.778	1.904	5.141
PBE-D2	AA	0.352	0.815	1.904	5.699
	AB	0.327	0.780	1.904	5.141
PBE-D3 (BJ)	AA	0.357	0.818	1.904	5.966
	AB	0.339	0.782	1.904	5.337

while other empirical potentials overestimate the diameter threshold at 6.0 and 6.2 nm [30,33]. This comes from the difficulty in accurately fitting the potentials over the wide length scale ranges required to accurately simulate a collapsed tube, and suggests empirical potentials are not well adapted for quantitatively modeling collapsed nanotubes.

The variation in DFT results come from the exchange-correlation energy functionals and dispersion corrections. The main difference between versions of GGA-D approximation is the interlayer spacing of the central zone, whereas the edge cavity height is largely independent of the dispersion correction implemented in the calculations. The central bilayer AB-stacking spacing using LDA matches experimental bilayer graphene (3.34 Å) [62,63], with GGA-D1(2) and D3(BJ) values close to previous calculations at similar levels of approximation [38,64].

Due to their weaker interlayer binding, the LDA and GGA functional without vdW interaction have larger edge cavities, 0.878 and 1.060 nm (0.895 and 1.078 nm) for AB (AA) stacking, respectively. Dispersion corrected GGA gives edge cavity heights of 0.780 (0.815 nm) for AB (AA) stacking independent of dispersion term used. These are very close to the diameter of a (6,6) nanotube (0.814 nm) and slightly larger than the diameter of C_{60} (∼0.7 nm) [65].

This analysis was extended to the zigzag (*n*,0) nanotubes. Our DFT-D2 calculations show the same threshold diameter for both armchair and zigzag configurations (see Fig. 2), confirming that the structural phase transition is large independent of tube chirality [17], with edge cavity slightly smaller than the diameter of a (11,0) nanotube (0.862 nm).

Hereafter we present only GGA-PBE(D2) calculations. This choice is based on both the interlayer description of graphite/bilayer graphene and self-collapse behavior of carbon nanotubes given in Appendix B. It shows the other DFT functionals as well as smaller basis sets (*pdpp*) all overestimate and underestimate key parameters: interlayer distances

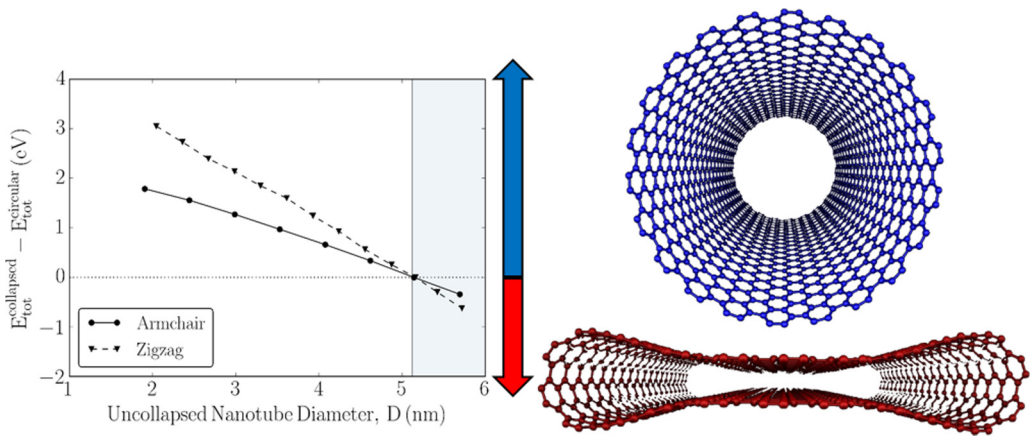

FIG. 2. Total energy difference between collapsed ($E_{tot}^{collapsed}$) and circular ($E_{tot}^{circular}$) nanotubes at different diameters with armchair (solid line) and zigzag (dashed line) chirality. Calculations are done for AB′-stacking orientation. Magenta section indicates diameters for which collapse is observed [17]. The threshold diameter for SWCNTs to collapse is essentially chirality independent (5.141 and 5.164 nm for armchair and zigzag, respectively).

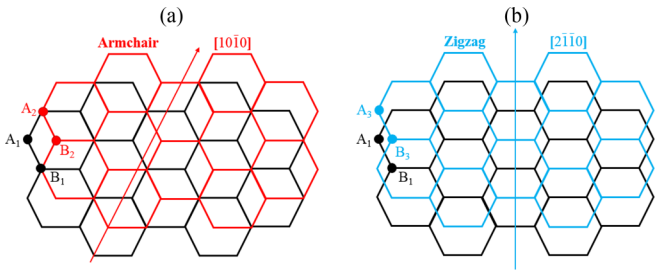

FIG. 3. Schematic showing the displacement along the (a) armchair and (b) zigzag direction of the lattice structures of facing layers forming the bilayer graphenelike central region of collapsed carbon nanotubes. Carbon atoms of the (black) lower and (red/blue) upper layers are denoted as $A_{1(2/3)}$ and $B_{1(2/3)}$, respectively.

and binding energies for graphite and bilayer graphene, and edge cavity heights and critical diameters for collapsed carbon nanotubes. Notably, carbon nanotubes never collapse using GGA-PBE without vdW corrections.

1. Geometry of collapsed SWCNTs with alternative interlayer stacking

The process of cross-sectional collapse lowers the symmetry of a carbon nanotube and introduces another degree of structural freedom, namely that of interlayer shearing in the central section, effectively "rolling" the tube in a similar way to a caterpillar track on a tank (see orange arrows in Figs. 1 and 3). This changes the stacking registry between the top and bottom layers.

While experimental studies suggest no apparent link between chiral angle and threshold diameter for collapse [17], theoretical studies on folded graphene see differences in collapse behavior with varying lattice registry [66]. In order to explore this point, we first calculated the interlayer binding energies for bilayer graphene with increasing translational shift along [10$\bar{1}$0] between adhering layers [see Fig. 4(a)]. As expected, for bilayer graphene the AB-stacked case corresponds to the most energetically favorable configuration, whereas translating along [10$\bar{1}$0], labeled as AB′, AA′, and AA [see Fig. 4(c)], increases the energy by ∼1, 6, and 10 meV/atom, respectively, showing the same trend as previous LDA studies on bilayer graphene [66].

Changing the stacking in the collapsed armchair nanotubes [via interlayer shearing in Fig. 4(b)], we see a similar trend in the collapse diameter threshold, which increases from 5.141 nm (AB and AB′ stacked, because the interlayer binding energy difference is only 1 meV) to 5.337 nm (AA′ stacked), reaching 5.699 nm when the central layers are AA stacked. The very smallest collapsed tubes in a stochastic width distributed sample should therefore have AB stacking. Assuming the larger diameter tubes have random chirality distributions, and then in general when they collapse they will produce turbostratic stacking, and hence AA′ stacking represents a better general model of collapsed carbon nanotubes than AA or AB.

2. Barrier to collapse of SWCNTs

We next analyze the structural pathway and saddle point energy associated with radial collapse of a (26,26) SWNT to

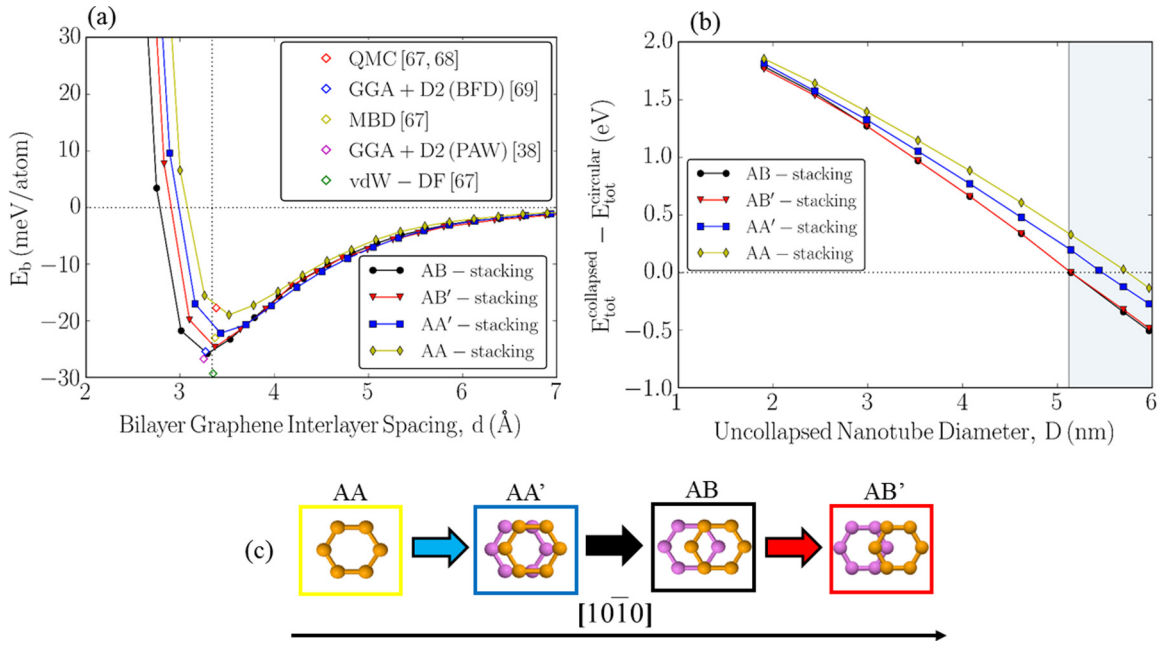

FIG. 4. (a) DFT-D2 calculated binding energies for bilayer graphene. Vertical line represents average interlayer distance of bilayer graphene obtained in recent experimental studies [63] and isolated points indicate different theoretical methods: GGA+D2 (PAW) [38], QMC, MBD, vdW-DF [67,68], and GGA+D2 (BFD) [69], respectively. (b) Total energy difference between free-standing ($E_{tot}^{collapsed}$) and circular ($E_{tot}^{circular}$) armchair (n, n) SWCNTs versus tube diameter D (nm). The intersection point at $\Delta E_{tot} = 0.0$ eV represents the threshold diameter for SWNTs to collapse. Shaded section indicates diameters for which collapse is observed experimentally [17]. (c) Structural motif for [10$\bar{1}$0] interlayer shear showing AA (yellow), AA′ (blue), AB (black), and AB′ (red).

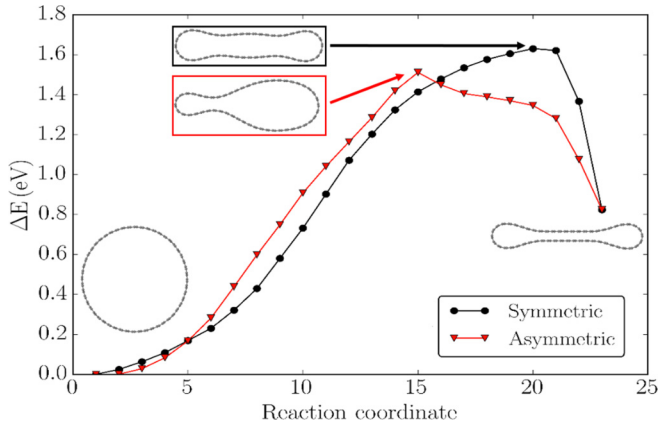

FIG. 5. Calculated symmetrical (black) and asymmetrical (red) reaction pathways for the collapse of a (26,26) SWCNT. The *y*-axis energy (eV) is the total energy difference per 104-atom unit cell compared to the stable tubular structure.

an AB-stacked collapsed structure (see Fig. 5). Two energy pathways were examined, a symmetric route where compressive strain was applied radially along a symmetry axis of the tube, and another with symmetry broken, allowing one edge cavity to form before the other.

The symmetric saddle point barrier is quite high at ∼1.6 eV, similar to previous literature values [33,38]. When symmetry is broken this barrier drops slightly to ∼1.48 eV, with the interlayer flattening starting next to the first cavity that forms and then propagating across the width of the nanotube. For larger tube diameters it is likely that the symmetric barrier will drop, since it is dependent on the curvature energy of the two tube halves at the point the top and bottom surfaces first touch. In contrast, the asymmetric route seems unlikely to change significantly and thus we suggest asymmetric collapse is only likely relevant for very small (and hence unstable) nanotube collapse. We note that these energies are per unit cell along the nanotube length, and due to the system periodicity assume simultaneous collapse along the whole nanotube length. In reality collapse is likely to occur at one or more local points along the tube and then propagate along its length.

B. Electronic properties of collapsed carbon nanotubes

Previous theoretical studies of armchair carbon nanotubes have shown that tube collapse induces a metal-semiconductor electronic phase transition, opening a small band gap [70,71]. This has been seen in conductance measurements with structural collapse by changing the temperature [10] and scanning tunneling spectroscopy (STS) spectra [72], demonstrating how nanotube collapse alters intrinsic electronic behavior without introducing topological defects, molecular adsorption, twisting or stretching, and may be used for example for nanoswitching applications [71]. The origin of this induced gap has been the object of intensive study. Tight-binding molecular dynamics (TB-MD) coupled with nonequilibrium Green's function (NEGF) calculations suggested it is induced by a combined effect of the weak interlayer interaction and symmetry breaking at the edges [71]. A similar transition was induced by squeezing a (6,6) carbon nanotube between two fixed graphene sheets using a self-consistent density functional tight-binding (SC-DFTB) approach [73].

1. Armchair collapsed carbon nanotubes with AA and AB stacking

We compare here the band structures of collapsed armchair (26,26) carbon nanotubes (2-CE-B-ZGNR, indicating "two closed edge bilayer zigzag graphene nanoribbons") with corresponding mono(bi)layer graphene nanoribbons, whose edges are saturated by hydrogen (M-ZGNR and B-ZGNR for the mono- and bilayer, respectively). We also include a bilayer graphene nanoribbon where one of the two edges is closed with interlayer bonding (similar to a collapsed tube), the other passivated by hydrogen. This gives essentially a folded graphene nanoribbon [74], referred to here as 1-CE-B-ZGNR.

For AB-stacked bilayer systems (B-ZGNR) we consider the α-edge alignment (interlayer translation imposed along the ribbon length), because it is energetically favorable with an associated edge distortion due to the attractive interaction between atoms [75]. The calculated edge interlayer distance is ∼ 0.301 Å (0.293 Å) for AB (AA) stacking, while the central zone interlayer spacing remains at 0.323 Å (0.347 Å) for AB (AA) stacking. Figure 6 shows the resultant band structures.

The single-layer M-ZGNR exhibits twofold degenerate bands around E_F as expected [76], localized edge states associated with the hydrogen passivated carbon atoms. The band structure of B-ZGNRs shows two important changes. First, the localized edge states couple between the layers, and separate away from E_F into bonding and antibonding pairs. Second the energy bands at the charge neutrality point are highly stacking dependent. For AB stacking we see the opening of a small gap (∼89 meV) and two parabolic bands (due to the interlayer coupling) with minima/maxima at $k \sim 2/3$. In contrast the AA stacking shows one parabolic band with wider gap at $k \sim 17/25$, with the appearance of a second linear band that approaches E_F at $k \sim 16/25$.

The 1-CE-B-ZGNRs show electronic structure intermediate between that of B-ZGNR and 2-CE-B-ZGNR, with one localized edge state from the hydrogen passivated edge resembling that of B-ZGNR, and the second edge state resembling that of 2-CE-B-ZGNR.

In contrast to the edge passivated structures, the collapsed armchair carbon nanotubes (2-CE-B-ZGNRs) show no edge-related states around E_F with band structures much more closely resembling those of infinite bilayer graphene. In the AB-stacked case the parabolic bands have minima/maxima at $k \sim 2/3$, with a subband gap opening of ∼180 meV. This is a signature of quantum confinement and interlayer coupling, which breaks the inversion symmetry between the layers, as seen in the wave function distribution, Fig. 6(a) right. This gap is higher than that of B-ZGNR (∼89 meV) and 1-CE-B-ZGNR (∼95 meV). The AA-stacked case has two states around E_F: a wide gap (∼300 meV) parabolic state with minimum at $k \sim 17/25$ and a linear band approaching E_F (semimetallic with a tiny gap of ∼15 meV) at $k \sim 16/25$. The wave function isosurface is distributed symmetrically with a higher concentration into the central region, because the interlayer coupling in this case does not break the inversion symmetry, as shown in Fig. 6(b) right. However, the asymmetrical AB configuration is energetically favorable over symmetrical AA stacking. This important result demonstrates

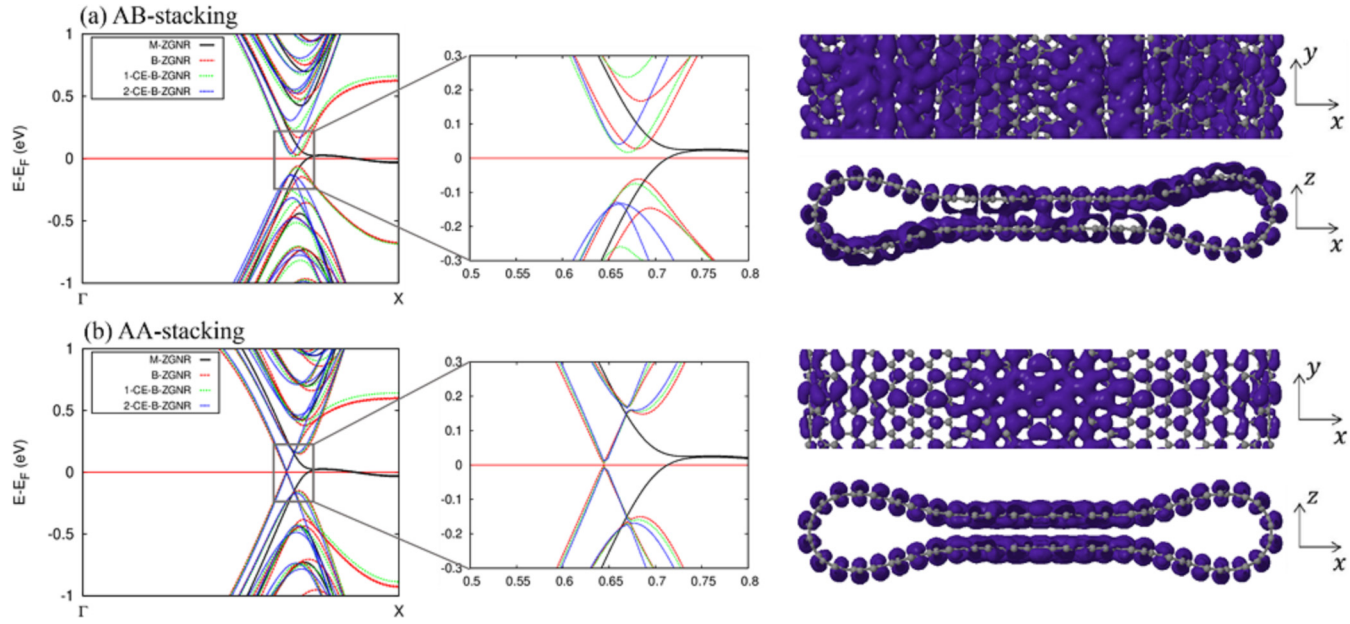

FIG. 6. (Left) Spin-averaged electronic band structures (purple) with (center) zoom of the bands at E_F and (right) square of the wave function isosurface for the occupied state in proximity to the charge neutrality point, both lateral and top view of an armchair (26,26) collapsed carbon nanotube (2-CE-B-ZGNR) and comparison with M-ZGNR (black), B-ZGNR (red), and 1-CE-B-ZGNR (yellow). (a) AB and (b) AA stacking.

the potential interest of collapsed carbon nanotubes of non-AB stacking as substituents for graphene nanoribbons, due to their linear dispersion and absence of edge states (with associated scattering and resistance) near the Fermi level.

For collapsed armchair CNTs (2-CE-B-ZGNRs), the shift of the Fermi level is due to charge transfer in the border area between curved regions and flattened bilayer where σ-π hybridization is enhanced [77].

Figure 7(a) shows the trend of energy band gap for AB-stacked armchair collapsed nanotubes as a function of the collapsed width W. It is possible to observe a second nanotube threshold diameter $D_{\text{flat}} \sim 3.5$ nm ($W = 5.09$ nm) such that

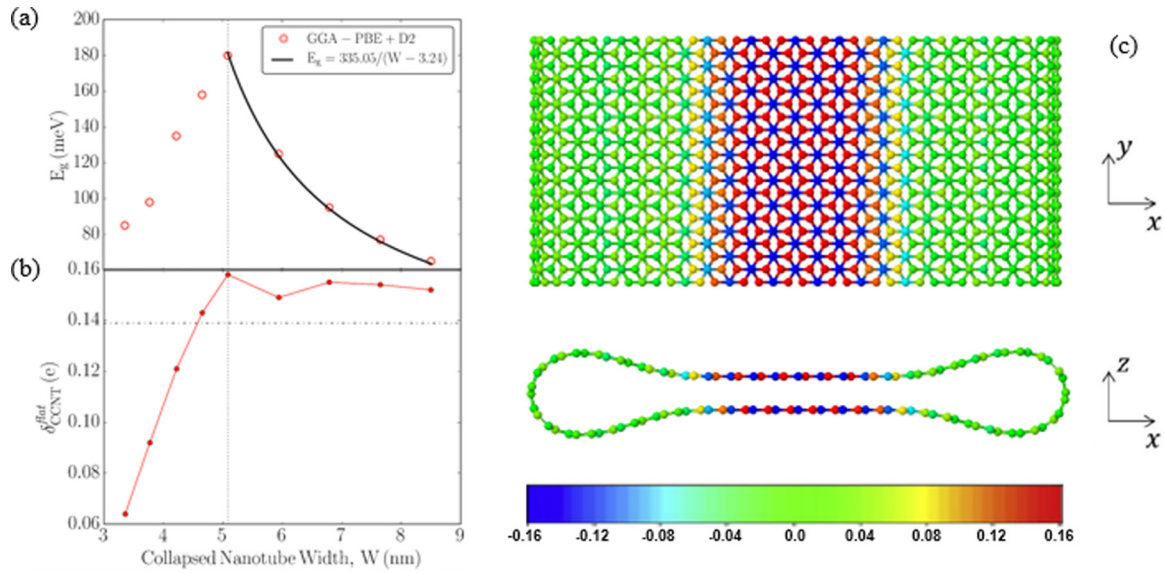

FIG. 7. DFT-D2 calculated (a) energy gaps (red empty circles) and (b) the maximum Mulliken positive charges located in the central region for AB-stacked flattened armchair (n, n) SWCNTs versus the collapsed nanotube width W_{total}. The solid black curve shows the equation $E_g(\text{meV}) = 335.05/(W - 3.24)$, fitted to the band gaps of the dogbone nanotubes. The new nanotube diameter threshold D_{flat} of ~3.51 nm ($W_{\text{flat}} = 5.09$ nm) is indicated by vertical dashed line. (d) Color representation of Mulliken partial charge distribution for a (26,26) AB-stacked collapsed tube with diameter corresponding to $D = D_{\text{flat}}$.

(1) $D \geqslant D_{\text{flat}}$: flattened nanotubes exhibit energy gaps *directly proportional* to their widths W. The bottom of the conduction band oscillates by roughly 35–40 meV, while the top of the valence band drops forming a gap. The same direct relationship is found for H@B-ZGNRs for widths <3.5 nm due to the geometrical deformation caused by the interlayer edge interactions [75]. There is only a very short poorly defined central region, as manifested in a geometric distortion of the entire tube structure. This is also reflected in the partial atomic charges δ determined via Mulliken population analysis, which show uniform charge distribution over the whole system [Fig. 16(a) in Appendix C].

(2) $D = D_{\text{flat}}$: the central region of (26,26) collapsed nanotube is well defined, with a band gap maximum of $\sim$ 180 meV. This is the most polarized nanotube, with partial atomic charges higher in the central region than the strained edge bulbs [Fig. 7(c)].

(3) $D > D_{\text{flat}}$: the energy gap is *inversely proportional* to width W, dependent on the increasing width of the well-defined central bilayer region. This inverse relationship comes from quantum confinement and the weak interlayer coupling. Our results are qualitatively in agreement with prior analytical calculations of the interwall potential by perturbation theory within the effective-mass approximation [78]. For wide semiconducting flattened SWCNTs, the electronic structure gradually approaches infinite AB-stacked bilayer graphene, as the bottom of the conduction band oscillates between 29–37 meV, while the top of the valence band rises reducing the energy gap. We expect the predicted band gaps will never disappear due to symmetry breaking caused by the edge bulbs. The Mulliken partial charges in the central flat zone of the collapsed nanotube approach asymptotically the positive/negative values ($\delta^{\pm}_{\text{BLG}} = \pm 0.139e$) of infinite AB-stacked bilayer graphene ($W \rightarrow \infty$) as determined via DFT-D2 [Figs. 7(b) and 17(b) in Appendix C].

This study demonstrates the direct correlation between charge transfer and band gap variation, whose origin can be fully explained: the interwall interactions in the strained edge bulbs are weaker (with interlayer distance of around 7.78–8.15 Å) than of the flattened region (3.27–3.52 Å). Because of different hybridization of π states of facing closed edges, they partially confine electrons in the bilayer graphene-like zone, resulting in a charge distribution difference between the parts which compose the whole system.

Quantum confinement and local charge effects due to the asymmetrical deformation geometry induce interlayer electrostatic polarization between facing layers such as to break the inversion symmetry, so that the interwall potential generates the band gap opening. This last point can be interpreted in terms of the different envelope wave functions between the top and bottom layer as ascribed to the boundary conditions at closed edges [79] and is viewable in the square of the wave function isosurface of Figs. 6(a) and 6(b). Note this new threshold diameter corresponds to the point at which a central bilayer graphenelike region begins to form, and is not indicative of thermodynamic stability (the thermodynamic stability cutoff will always be larger).

For $D \geqslant D_{\text{flat}}$ the energy gaps (eV) can be fitted by $E_g = 335.05/(W - 3.24)$. In this case 3.24 nm gives an effective width of the two edge cavities (i.e., 1.62 nm per cavity). We note that the diameter of the edge cavities is width independent and very close to that of a (6,6) circular carbon nanotube. Indeed from $D = D_{\text{cross}} = 5.141$ nm and above, the partial atomic charges around the edge cavities are almost identical to our calculated nanotube value of $\pm 0.01e$. Similar values were obtained using the Bader method to calculate the atomic charges.

Thus in summary, for armchair nanotubes at or above the threshold diameter for collapse, collapse into AB stacking results in a finite band gap inversely proportional to the nanotube diameter, due to the lateral confinement of the electrons. For tubes with smaller diameters this trend undergoes an inversion at a new diameter threshold D_{flat}, at which point edge cavity behavior dominates. D_{flat} lies below the collapse stability threshold D_{cross} so it will not normally be experimentally observable.

The partial atomic charges in infinite AA-stacked bilayer graphene are close to zero, as the interlayer coupling does not break the inversion symmetry. However, charge distributions in the corresponding collapsed nanotubes are instead polarized similar to the AB case, due to symmetry breaking by the tubular edges, with corresponding electronic confinement and charge distribution variation. In the AB-stacked case the polarization across the central zone is uniform, corresponding to the finite parabolic semiconducting gap. However in the AA case this is complicated by the linear semimetallic Dirac-like bands, which superimpose a width-dependent charge wave on the central ribbon section. The result is polarized lines along the ribbon length of highly charged ($\sim \pm 0.17e$) and more weakly charged ($\sim \pm 0.05e$) carbon atoms. The onset of polarization in the central zone (D_{flat}) occurs at the same value, 3.5 nm, as in the AB-stacked case, suggesting D_{flat} is stacking independent, unlike D_{cross}.

For the AA-stacked tubes the semimetallic band gap remains independent of nanotube diameter at $\sim 15 \pm 3$ meV. The secondary parabolic bands at $k \sim 17/25$ show an inverse relationship to width similar to the AB-stacked case, this time varying as $E_g = 437.58/(W - 3.20)$. Both the B-ZGNRs and AA-stacked collapsed tubes show a wider energy variation for this parabolic band than the corresponding AB-stacked case.

2. Armchair collapsed carbon nanotubes with intermediate stacking

For the intermediate case between AA and AB stacking (labeled AA′), the band structure is also intermediate between AA and AB. Two parabolic bands approach the Fermi level at k vectors slightly above and below $k = 33/50$ (the K point), each with an associated band gap. These gaps vary differently with nanotube size [see Figs. 8(a)–8(c)]. The energy gap at lower k, E_g^L, increases with width/diameter (with bands which are nearly linear except near to the gap), while the energy gap for the band at higher k, E_g^H, decreases with values nearly equal to those obtained for AA stacking.

For a final intermediate stacking (AB′, where the translation vector from AB to AA′ is inverted), the system is semimetallic. The lowest conduction state drops below E_F for width $W = 5.06$ nm and continues to drop with increasing width [see Figs. 8(d)–8(f)].

Additionally, another size-dependent effect is seen, namely electron-hole asymmetry (similar to behavior in AB). This

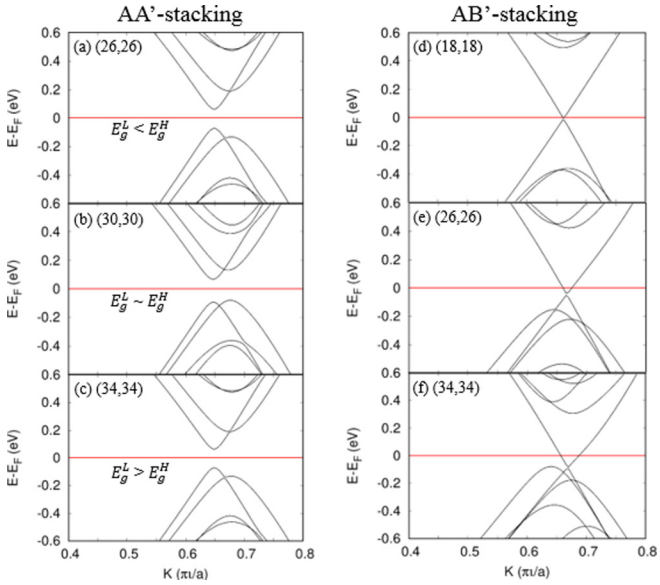

FIG. 8. Spin-averaged electronic band structures of armchair (n,n) collapsed carbon nanotubes (2-CE-B-ZGNR) in intermediate AA′ stacking (left column, with $n = 26$, 30, 34) and AB′ stacking (right column, with $n = 18$, 26, 34).

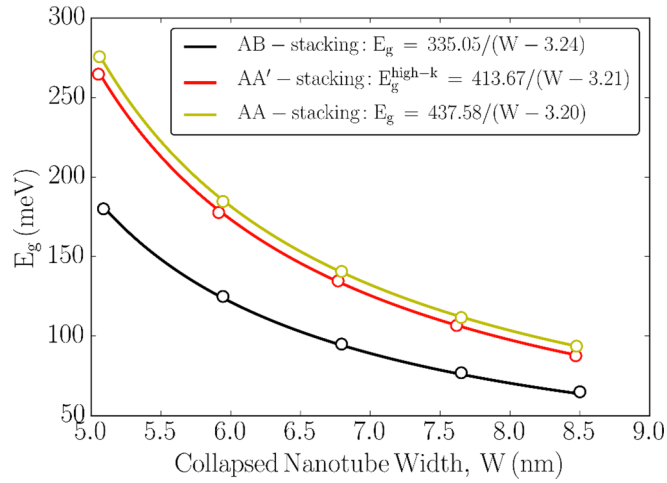

FIG. 9. DFT-D2 calculated energy gaps (empty circles) for collapsed armchair (n, n) SWCNTs versus collapsed nanotube width W with AB (black), AA′ (red), AA (yellow) stacking. The solid curves show the best-fit equations: $E_g(\text{meV}) = 335.05/(W - 3.24)$, $E_g(\text{meV}) = 413.67/(W - 3.21)$ and $E_g(\text{meV}) = 437.58/(W - 3.20)$ for AB, AA′, and AA interlayer stackings, respectively. AA′ also has a smaller low-k gap which does not follow this same trend (see text).

should be detectable in quantum Hall regime transport measurements [80]. Dirac fermions will be present over a larger energy window in AB′ than in monolayer graphene, without being perturbed by conventional Fermi carriers coming from the parabolic bands. Such electronic structures are examples of how different effects are simultaneously in play, underlining the heavy dependence on the stacking and registry effects.

In summary, the conduction and valence states around the Fermi level of collapsed armchair nanotubes depend to a great extent on the interlayer translation and associated stacking between the top and bottom layer. There are always two bands near the Fermi level around $k = 2/3$ (the K point). In AA stacking the first of these manifests as a crossed linear band with a few meV gap at the Fermi level, the other at higher k as a wide-gap parabolic band. As the stacking shifts towards AB the character and gap of these bands change until at AB stacking both bands are parabolic with intermediate gaps.

In general, the gap of these bands, when parabolic, is inversely proportional to $(W_{\text{total}} - x)$ due to quantum confinement and local charge, where W_{total} is the total width of the collapsed nanotube and x is approximately constant and corresponds to the combined width of the two collapsed ribbon cavities (around 3.2 nm). The precise scaling rule depends on the stacking as shown in Fig. 9. Although the smaller low-k gap in AA′ stacking does not follow this trend, the secondary high-k parabolic band follows the $\sim 1/W$ trend and is included in Fig. 9 for completion.

Unlike grafold [66], the electronic structure of collapsed tubes with different stackings do not show indirect band overlap. However, in grafold there are three or more stacked layers with a variety of simultaneous stacking configurations possible, and it would be interesting to see whether such effects appear when collapsed tubes are placed on graphene substrates or in bundles. We note that the electronic structures reported here neglect charge transfer process due to substrate interactions [81,82], which are likely to affect measurements made with scanning tunneling microscopy (STM) and scanning tunneling spectroscopy (STS) [83–85], and can show Fermi-level shift depending on the work function difference between the tube and substrate [86]. They also do not incorporate the effect of twisting or kinks that can degrade the conductivity, as observed in previous Raman measurements [16].

In general, the gaps are systematically higher than other equivalent-width bilayer configurations and do not have edge-related states around the Fermi level, suggesting they may be promising substitutes for related systems such as hydrogen terminated conductive graphene nanoribbons.

3. Zigzag collapsed carbon nanotubes

In the previous section we have considered in detail the electronic structure of armchair collapsed nanotubes. To the best of our knowledge, theoretical analysis of comparable zigzag collapsed nanotubes has not previously been reported.

The electronic structure of circular CNTs with zigzag chirality is more complicated than their armchair (metallic) counterpart, because this nanotube family can be split into three types as a function of diameter. While $(3n, 0)$ tubes show metallic conductivity, $(3n + 1, 0)$ and $(3n + 2, 0)$ tubes are semiconducting, with the opening of a band-gap as follows: $E_g^{3n+2} > E_g^{3n+1} > E_g^{3n}(= 0)$ for all n [87].

A similar classification is also found for hydrogen terminated mono- and bilayer armchair graphene nanoribbons (AGNRs). Although there are not metallic nanoribbons, they exhibit three distinct sets of energy gap: $E_g^{3p+1} > E_g^{3p} > E_g^{3p+2}$, as a function of the ribbon width $[(3p + x)$ carbon dimer lines, if the ribbon is considered as an unzipped nanotube then $p = n/2]$ [88,89]. This classification is either understood in terms of quantum confinement combined with hydrogen

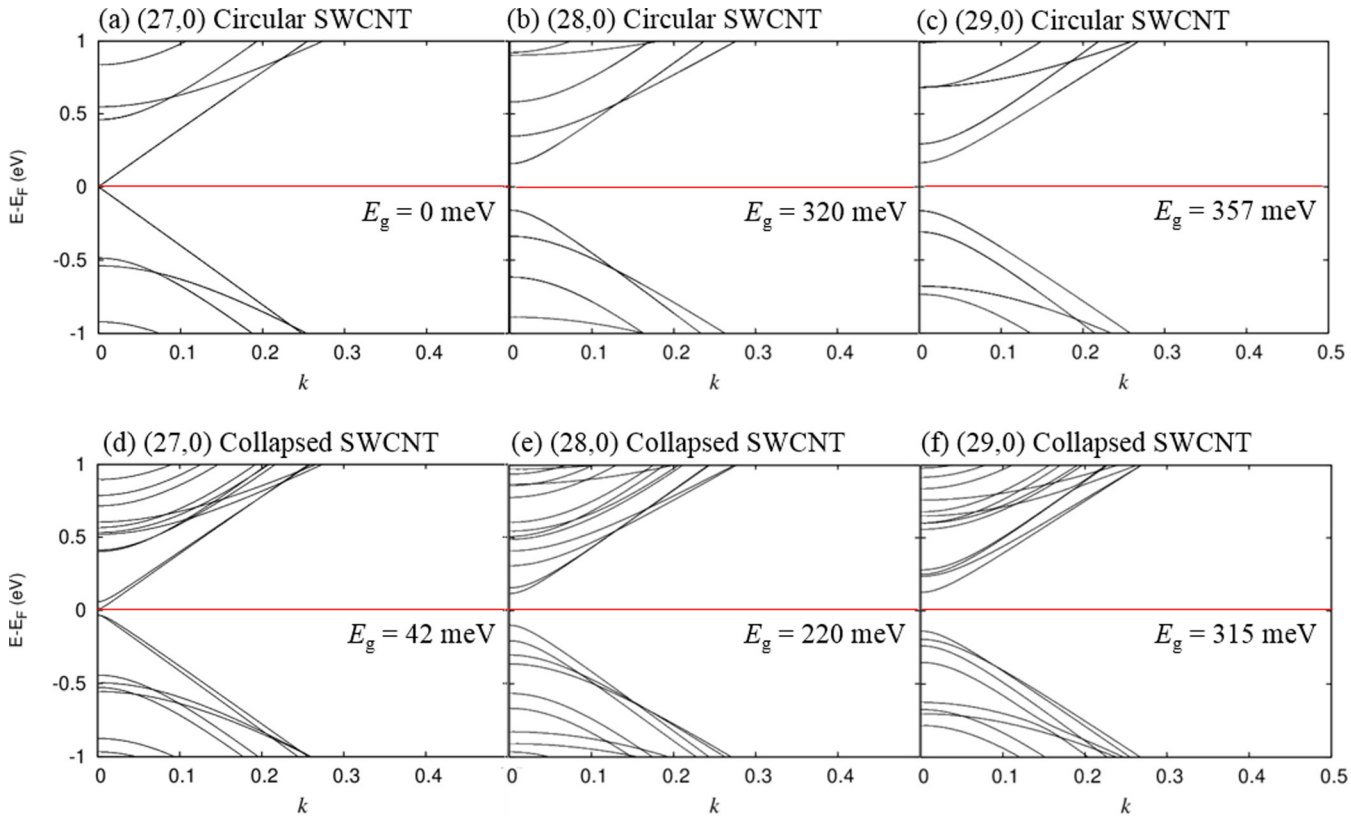

FIG. 10. Spin-averaged electronic band structures of zigzag $(n,0)$ circular (upper panel) and collapsed (lower panel) single-walled carbon nanotubes with $n = 27$ (a) and (d), 28 (b) and (e), and 29 (c) and (f). Fermi level is indicated by solid red line.

edge termination effects, i.e., σ bonds, and on-site energies of edge carbon atoms differ from those in the central region of the ribbon [88–90]. Alternatively a more chemical description using Clar sextet theory is used, rationalizing the armchair ribbons into three structural representations corresponding to fully benzenoid, Kekulé, and incomplete Clar structures [91].

We find that zigzag collapsed carbon nanotubes with AB′ central stacking can also be classified in three families (see Fig. 10). The $(3n,0)$ circular nanotubes are semiconductors with zero band gap (similar to graphite) at the Dirac point, while their equivalent collapsed tubes exhibit small energy gaps. This is analogous with the corresponding armchair case, demonstrating that the metallic-semiconductor electronic transition due to radial deformation of circular tubes is largely independent of tube chirality. The $(3n+1,0)$ and $(3n+2,0)$ nanotubes remain semiconducting upon collapse, with gaps comparable to those of cylindrical tubes. The collapsed SWCNTs show the same sequence of energy gaps as their equivalent circular counterparts.

Similar to the armchair case, we compared the electronic structure of circular zigzag nanotubes with M(B)-AGNRs, and collapsed zigzag SWCNTs by varying the chiral index (or the equivalent number of dimer lines), as shown in Appendix D, Fig. 17. While the circular tube bands are fully linear at E_F, the bilayer hydrogen-terminated ribbons show local band curvature, and the collapsed tube has intermediate character, remaining largely linear.

Like the armchair dogbone nanotubes, the resulting energy gaps of $(3n,0)$, $(3n+1,0)$, and $(3n+2,0)$ zigzag collapsed SWCNTs with a substantial central flat region are inversely proportional to their widths, with different fit models: $E_g(\text{meV}) = 23.21/(W-3.31)$, $E_g(\text{meV}) = 51.72/(W-3.31)$, $E_g = 83.25/(W-3.31)$ for $(3n,0)$, $(3n+1,0)$, and $(3n+2,0)$ subfamilies, respectively (see Fig. 11). The threshold diameter for thermodynamically favored

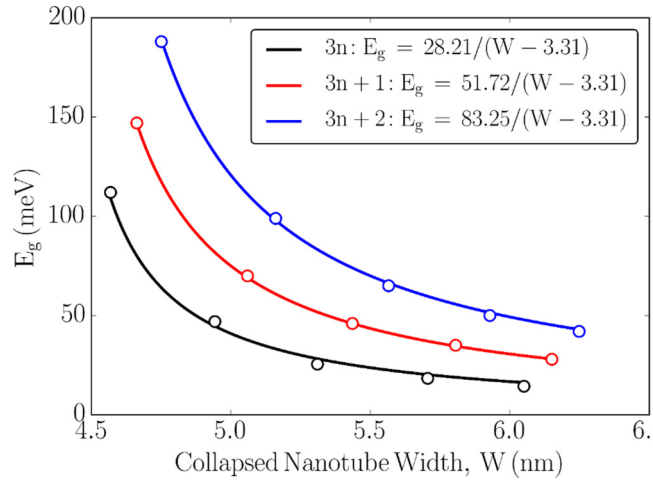

FIG. 11. DFT-D2 calculated band gaps of semiconducting zigzag $(3n,0)$, $(3n+1,0)$, and $(3n+2,0)$ collapsed carbon nanotubes (empty circles) versus width. The solid curves show the best-fit equations: $E_g(\text{meV}) = 28.21/(W-3.31)$, $E_g(\text{meV}) = 51.72/(W-3.31)$, and $E_g(\text{meV}) = 83.25/(W-3.31)$ for $(3n,0)$, $(3n+1,0)$ and $(3n+2,0)$ nanotubes, respectively.

collapse for zigzag nanotubes is $D \geqslant 5.16$ nm, the same as their armchair counterparts. However, the electronic structure and scaling rules of the energy gap are quite different and follow qualitatively the difference in behavior seen in armchair and zigzag carbon nanotubes, i.e., this difference can be ascribed to the different chiralities and associated 1D-confinement induced band folding of the bilayer graphene band structure.

Semilocal exchange-correlation functionals such as GGA-PBE with vdW forces used in our current study likely systematically underestimate the semiconducting band gaps. Literature studies for metallic carbon nanotubes show GGA-PBE underestimates small meV gaps, while higher level GW-corrected LDA overestimates them [92]. Nonetheless, in experimental temperature measurements of conductance at the Dirac point for ∼20 nm width tubes find an estimated transport gap of 13.7 meV [10], between our calculated prediction for armchair (21.2 meV) and zigzag (3.27 meV) dogbone nanotubes. The qualitative $1/W$ trend of E_g is in agreement with prior calculations on hydrogen-edge terminated GNRs using methods beyond DFT such as Green's functions and screened Coulomb interaction [93].

In summary, we demonstrate that all considered carbon nanotubes (armchair and zigzag) including all subfamilies (depending on the chiral index/number of dimer lines) become semiconductors upon collapsing, mainly due to the confinement and charge transfer process of carbon atoms from strained edge cavities and qualitatively confirmed by electrical transport measurements of field-effect transistors based on narrow graphene nanoribbons with ultrasmooth edges [94].

IV. CONCLUSIONS

We have systematically studied the radial collapse of single-walled carbon nanotubes using various theoretical techniques, showing that of those tested, the GGA exchange-correlation functional with Grimme dispersion corrections gives the most reliable results. The threshold diameter for free-standing SWCNTs to collapse depends on two parameters: the original nanotube chirality and the interlayer registry dependence, a new variable introduced to the nanotube due to the symmetry breaking induced by its collapse. The registry can be modified through interlayer shear (equivalent to rotation of the original tube about its axis). Our calculated threshold for collapse with AB stacking is 5.1 nm, in good agreement with available experimental data, rising to 5.3 nm for more representative intermediate stacking (AA′).

We introduce a new threshold diameter D_{flat} (∼3.5 nm) below the threshold diameter, at which a flattened central zone is first apparent. It is largely chirality independent and can be quantified via a turning point in the calculated band gap dependence with diameter, as well as the emergence of charge polarization in the collapsed tube central zone.

We have investigated the electronic structure of armchair and zigzag collapsed nanotubes. Armchair collapsed nanotubes all show the appearance of a small band gap due to confinement in the flat central zone induced by the curved edges. Band gap size and band structure around the Fermi level are both strongly registry dependent. Similar to zigzag nanotubes and graphene nanoribbons, zigzag collapsed nanotubes form three distinct small-gap semiconductor families depending on their widths, with band gaps $\leqslant 0.3$ eV. All collapsed tubes show an inverse relation between band gap and tube width, independent of chirality. The knowledge of the effects due to the slight displacements between two layers and the tube topology is a crucial issue to control the experimental conditions of the formation of collapsed carbon nanotubes of desired energy gap, which can be measured by STM and STS. This is of great interest to engineer suitable band gaps for applications using these deformed carbon nanotubes.

Collapsed carbon nanotubes show many potential advantages over equivalent edge-functionalized graphene nanoribbons and conventional carbon nanotubes. These include an absence of electronic states around the Fermi level associated with ribbon edge states, uniform smooth edges along their length minimizing scattering, and linear bands near the Fermi level. This suggests that collapsed carbon tubes should make highly promising substitutes for nanoribbons and circular nanotubes in nanoelectronics and spintronics applications.

ACKNOWLEDGMENTS

We thank D. V. Rybkovskiy, P. Puech, Y. Sayed-Ahmed-Baraza, and J. Rio for stimulating discussions. This work received funding from the French Agence Nationale de Recherche Project ANR-16-CE24-0008-01 "EdgeFiller." We acknowledge the CCIPL "Centre de Calcul Intensif Pays de la Loire" where many of the calculations were performed.

TABLE II. Equilibrium interlayer distance d_{int} (in nm), binding energy E_b (in meV/atom) obtained using LDA and GGA-PBE implementing various versions of van der Waals corrections for graphite and bilayer graphene in both AA- and AB-stacking styles.

	Graphite				Bilayer graphene			
	AB		AA		AB		AA	
Method	d_{int}	E_b	d_{int}	E_b	d_{int}	E_b	d_{int}	E_b
LDA	0.332	−28.85	0.358	−18.51	0.332	−16.61	0.358	−9.55
PBE	0.445	−2.91	0.460	−2.57	0.410	−1.33	0.438	−1.28
PBE+D1	0.321	−54.31	0.346	−40.56	0.325	−26.28	0.350	−18.50
PBE+D2	0.323	−54.96	0.347	−41.77	0.327	−26.30	0.352	−18.51
PBE+D3 (BJ)	0.337	−51.03	0.350	−41.22	0.339	−24.22	0.357	−14.92

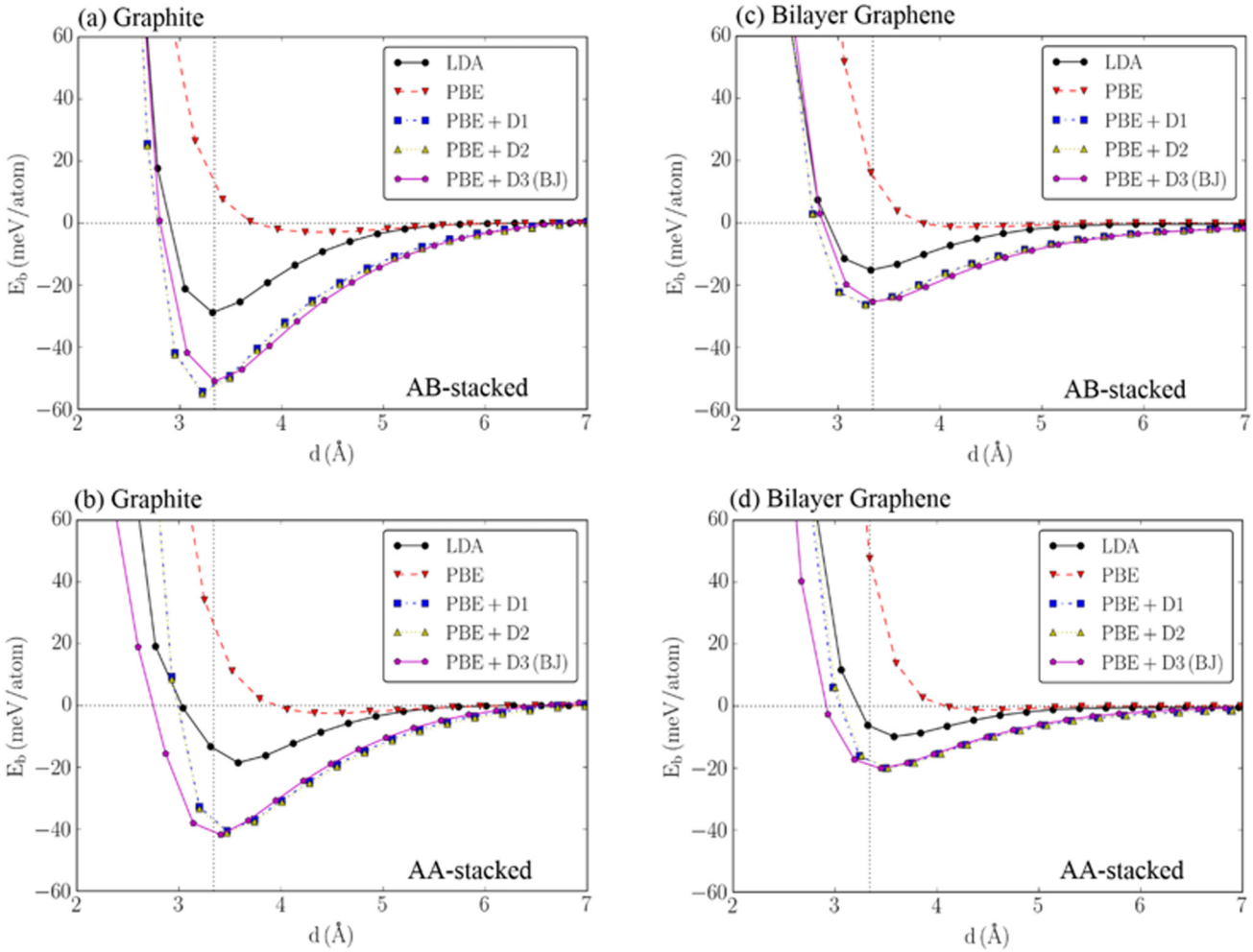

FIG. 12. Interlayer binding energy of graphite (left column) and bilayer graphene (right column) in both AB (upper panel) and AA (lower panel) stacking styles by changing the approximation for the exchange-correlation DFT functional. Vertical dashed line represents experimental interlayer distance of graphite and bilayer graphene [62,63].

APPENDIX A: INTERLAYER INTERACTIONS IN GRAPHITE AND BILAYER GRAPHENE

Many functionals in graphitic systems are optimized to correctly model the interlayer binding and spacing in graphite. In collapsed carbon nanotubes however, larger interlayer spacing in the 3.5–7 Å range also come into play, in the curved region between the flat central section and the tubelike edges. The interlayer spacing increases continuously here, and as such the precise form of the interlayer potential curve can strongly modify the structure and binding energy. This has the knock-on effect of modifying the resultant edge cavity height. Additionally, the energetics of the well depth are critical in order to correctly model the energy balance in collapsed nanotubes between edge curvature energy and interlayer attraction in the central zone. In order to better understand the behavior of different levels of theory in this region as we vary interlayer spacing, we modeled infinite graphite as well as bilayer graphene, in both AA- and AB-stacking configurations. To describe the graphene-graphene interaction and comparing with literature satisfactorily, all common exchange-correlation functionals are tested. The vacuum is set in order to have a separation distance around of 3.34 Å (>15.0 Å) for graphite (bilayer

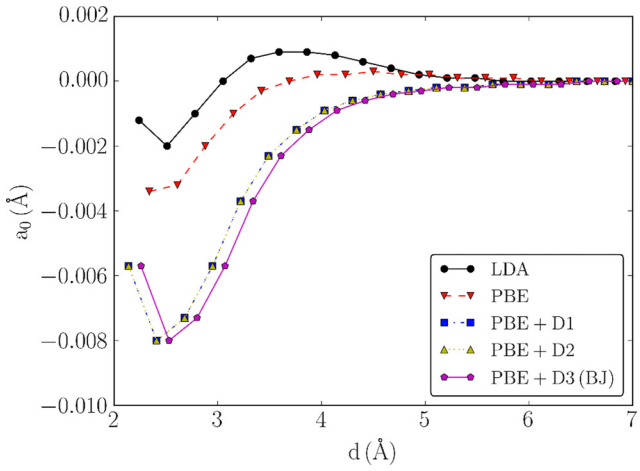

FIG. 13. Variation in geometrically optimized unit cell length along the periodic direction as a function of minimum interlayer spacing for AB-stacked graphite (graphene bilayer). Below a given interlayer distance cutoff ∼2.41 Å (as represented by vertical dashed line), lattice vector increases because the C atoms between two layers tend to bound forming eventually strained diamond.

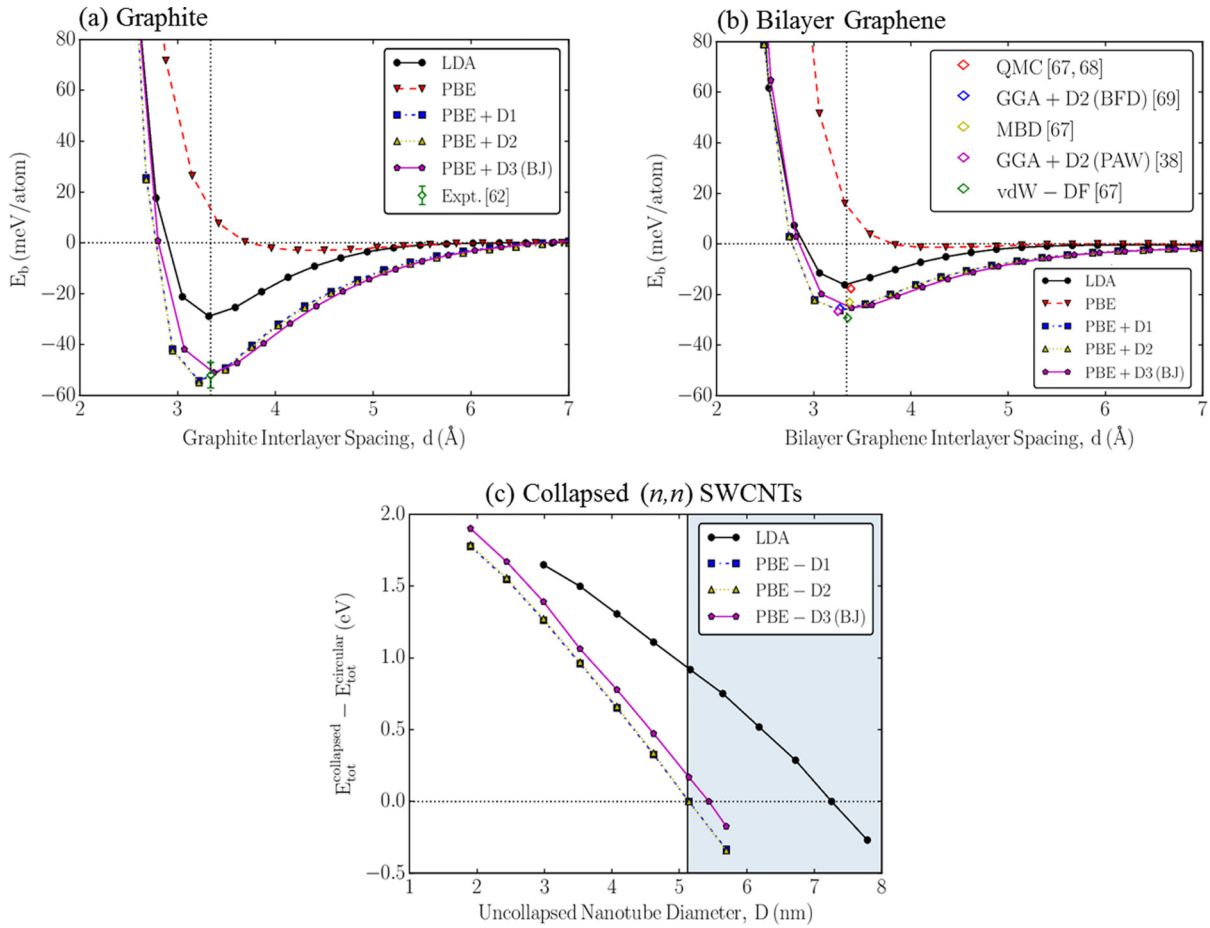

FIG. 14. DFT calculated interlayer binding energies for AB-stacked graphite (a) and bilayer graphene (b) in comparison with experiment (52 ± 5 meV) [62,63] and different theoretical methods: GGA+D2 (PAW) [38], QMC, MBD, vdW-DF [67,68], and GGA+D2 (BFD) [69], respectively. Vertical dashed line represents interlayer distance of graphite and bilayer graphene obtained in the experiment [62,63]. (c) Total energy difference between free-standing collapsed ($E_{\text{tot}}^{\text{collapsed}}$) and circular ($E_{\text{tot}}^{\text{circular}}$) armchair (n, n) SWCNTs versus tube diameter D (nm). The intersection point at $\Delta E_{\text{tot}} = 0.0$ eV represents the threshold diameter for SWNTs to collapse. Shaded section indicates diameters for which collapse is observed experimentally [17]. All calculations are carried out on AB-stacked structures with a large *pdddp* basis set.

graphene). The k mesh in the first Brillouin zone was set to be $24 \times 24 \times 12$ (1) for graphite (bilayer graphene), and the convergence of total energy was 1×10^{-7} eV. Unit cell and atom positions were allowed to relax.

Such modeling was employed to obtain the lowest binding energies E_b for all cases here reported (see Table II). At each point on the curves the interlayer spacing is fixed and the in-plane lattice constants are then allowed to fully relax (see Fig. 12).

For graphite, the binding energies at equilibrium separation for the GGA+D results predicted by *pdddp* basis set are in good agreement with most recent theoretical results [62–64] and are nearly identical to experiment within measurement uncertainty [62]. For bilayer graphene, the DFT-D results calculated by *pdddp* basis set are somewhat larger (in magnitude) than those obtained by using quantum Monte Carlo (QMC) method [67,68], whereas they are very close with the vdW correction based on self-consistent nonlocal electron correlation (vdw-DF) and many-body dispersions (MBD) referred to in Ref. [67] and match with the most recent density functional calculations (within the Grimme scheme) using plane-wave basis set (GGA+D2-PAW) [38] or pseudopotentials proposed by Burkatzki, Filippi, and Dolg (GGA+D2-BFD) [69].

Note that at each interlayer spacing the in-plane lattice vectors are always re-optimized but this changes energies by less than 1 meV compared to the nonrelaxed case. Below a given minimum interlayer spacing (slightly dependent on the DFT approximation), the lattice vector along the periodic direction increases and the layers eventually crosslink, forming strained bilayer diamond (see Fig. 13).

As expected, it is only under compression that we see differences in the interlayer binding energy between D1/D2 and D3, since D3 dispersion corrections are modified to better account for high pressure interaction. In summary, while LDA and GGA show significant deviation from experimental behavior there is little difference between the dispersion corrected GGA results, which in general give good match to experiment in terms of equilibrium interlayer spacing, as well as interlayer binding energies from the equilibrium spacing and above.

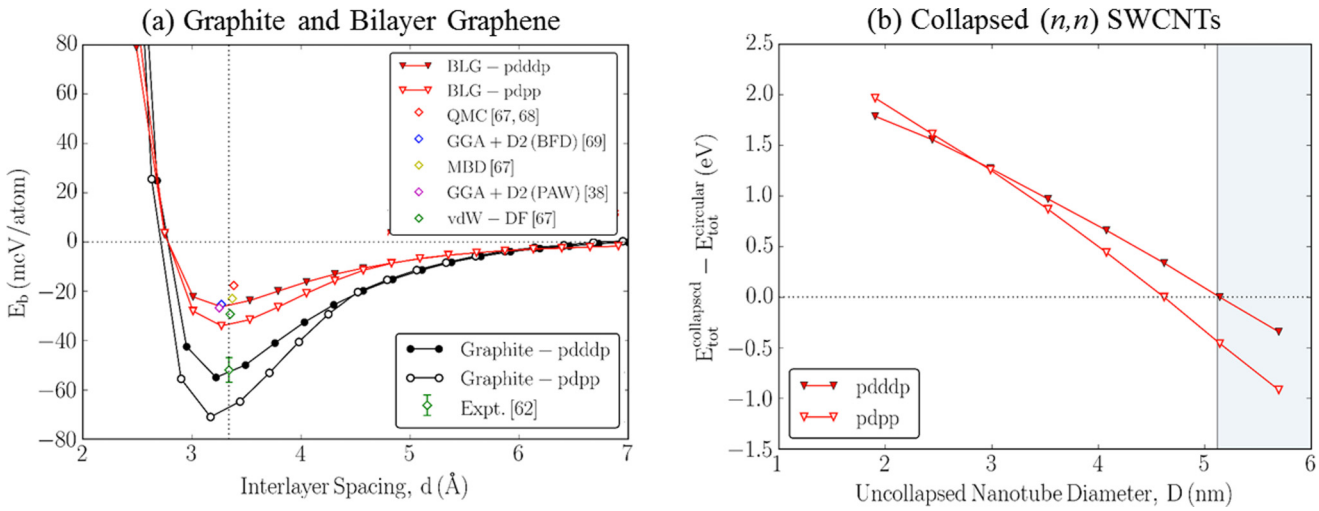

FIG. 15. Effect of changing basis set from a complete *pdddp* set (filled) to a smaller *pdpp* set (empty). DFT-D2 calculated binding energies for AB-stacked graphite and bilayer graphene (a) and their comparison with experiment (52 ± 5 meV) [62,63] and different theoretical methods: GGA+D2 (PAW) [38], QMC, MBD, vdW-DF [67,68], and GGA+D2 (BFD) [69], respectively. Vertical dashed line represents interlayer distance of graphite and bilayer graphene obtained in the experiment [62,63]. (b) Corresponding total energy difference between free-standing collapsed ($E_{\rm tot}^{\rm collapsed}$) with different cross sections and circular ($E_{\rm tot}^{\rm circular}$) armchair ($n$, n) SWCNTs versus tube diameter D (nm). The intersection point at $\Delta E_{\rm tot} = 0.0\,$eV represents the threshold diameter for SWNTs to collapse. Shaded section indicates diameters for which collapse is observed experimentally [17].

APPENDIX B: COMPARISON OF PERFORMANCE OF DFT FUNCTIONALS AND BASIS SETS FOR SELF-COLLAPSING OF SWCNTs

The experimentally measured diameter for free-standing tube collapse of 5.1 nm [17], measured on collapsed tubes with stacking close to AB, exactly matches with our AB-stacked GGA+D2 results [Fig. 14(c)]. The variations in this threshold with exchange-correlation and dispersion functionals can be understood through examination of the interlayer binding for graphite and bilayer graphene [Figs. 14(a) and 14(b)]. There is a clear correlation between binding energy minima in Figs. 14(a) and 14(b) and collapse threshold diameter [Fig. 14(c)]. While GGA+D2 matchs well the experimental threshold, LDA overestimates this due to underestimation of the interlayer binding energy, and it is not possible to obtain stable collapsed tubes with non-vdW corrected GGA because the interlayer binding is so weak.

In summary, the collapsed geometries obtained from GGA+D2 show the best agreement with available experimental data, and where available agrees with prior literature at the same level of theory. LDA calculations underestimate the interlayer interaction and hence overestimate the collapse diameter and edge cavity sizes. Underestimation of the interlayer potential of the GGA without dispersion corrections is so high that the collapse diameter cannot be reached and cavity height is highly overestimated. The AIREBO empirical potential underestimates the collapse threshold diameter and cavity size.

The precise diameter threshold value for nanotube collapse is sensitive to many factors, and there is significant variation in literature calculations of collapsed carbon nanotube geometry [5,7,16,17,29–39], even for calculations using apparently the same level of theory. For example, previous literature GGA-D2 calculations using a plane-wave basis set with a cut-off energy of 400 eV reported larger AA-stacked cavity sizes (0.854 nm) than ours [38]. In order to explore the influence of basis set further we re-optimized everything with a smaller *pdpp* set (dropping from 38 independent Gaussian-based functions per atom to 22).

Focusing on the GGA-D1/2 case, reducing the basis set size reduces the threshold diameter from 5.699 to 5.337 nm for AA stacking, and 5.141 to 4.618 nm for AB stacking. This brings the AA-stacked result into agreement with Ref. [38], suggesting the difference in our results is due to our more complete basis sets. The central interlayer spacing is largely unchanged and remains approximately equal to the interlayer separation of turbostratic graphite, whereas the cavity heights increase by a maximum of ∼0.06 nm (again matching [38]). This dependence on basis set can be understood by examining the spacing dependent interlayer interaction both in graphite and bilayer graphene using the two basis sets and comparing it with total energy difference between circular and flattened nanotubes (see Fig. 15). While both basis sets are able to reproduce roughly the interlayer spacing at equilibrium, the interlayer binding energies predicted by *pdpp* basis set are lower than the *pdddp* values. Thus the smaller basis set will overestimate interlayer interaction in the central flat region and thus also overestimate the stability of the collapsed structures. The same effect was seen using the D3(BJ) correction.

This demonstrates that edge cavity height and diameter collapse threshold are strongly dependent on the exchange-correlation functional and the basis set implemented and that GGA-D2 coupled with *pdddp* basis set represents the best theoretical scheme to better investigate free-standing single-walled carbon nanotubes characterized by collapsed shape.

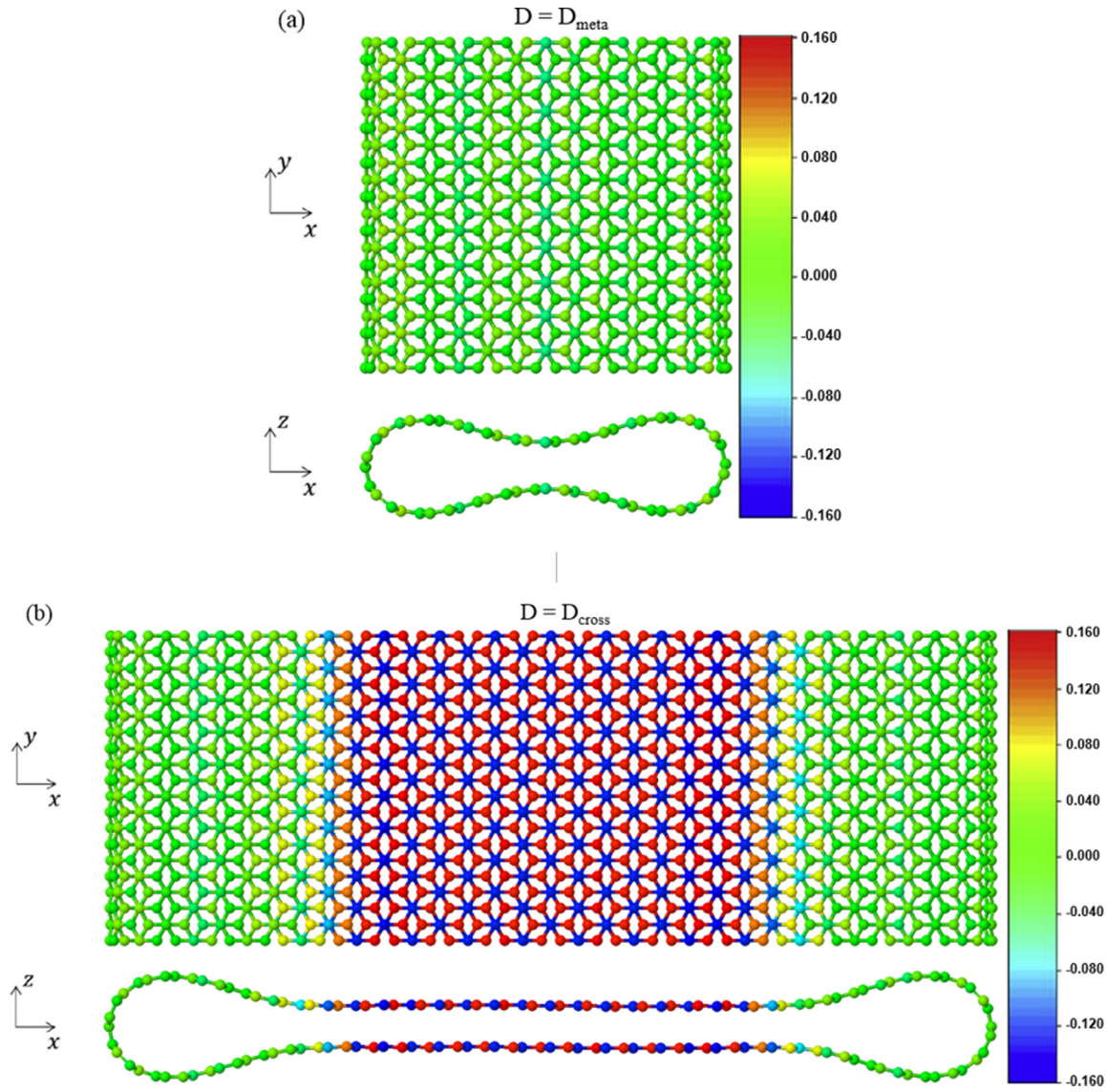

FIG. 16. Color representations of Mulliken partial charge distribution for (14,14) and (38,38) AB-stacked collapsed nanotubes whose diameters are equal to $D = D_{\text{meta}}$ (a) and $D = D_{\text{cross}}$ (b) from top and lateral view.

APPENDIX C: MULLIKEN POPULATION ANALYSIS OF COLLAPSED SWCNTs

Figure 16 shows color representations of the calculated Mulliken partial charge distribution for (14,14) and (38,38) AB-stacked collapsed nanotubes, showing the change in central charge distribution at the two transitions, $D = D_{\text{meta}}$ and $D = D_{\text{cross}}$. Charge distribution in the central region of the second case closely matches that of AB-stacked bilayer graphene.

APPENDIX D: QUASIPARTICLE ENERGIES AND BAND GAPS OF ARMCHAIR MONO(BI-)LAYER GNRs AND ZIGZAG SINGLE-WALLED CNTs

Figure 17 shows spin-averaged electronic band structures of sequentially increasing width/diameter for monolayer (first row) and bilayer (second row) armchair graphene nanoribbons, with third row showing similar sequence for collapsed zigzag nanotubes.

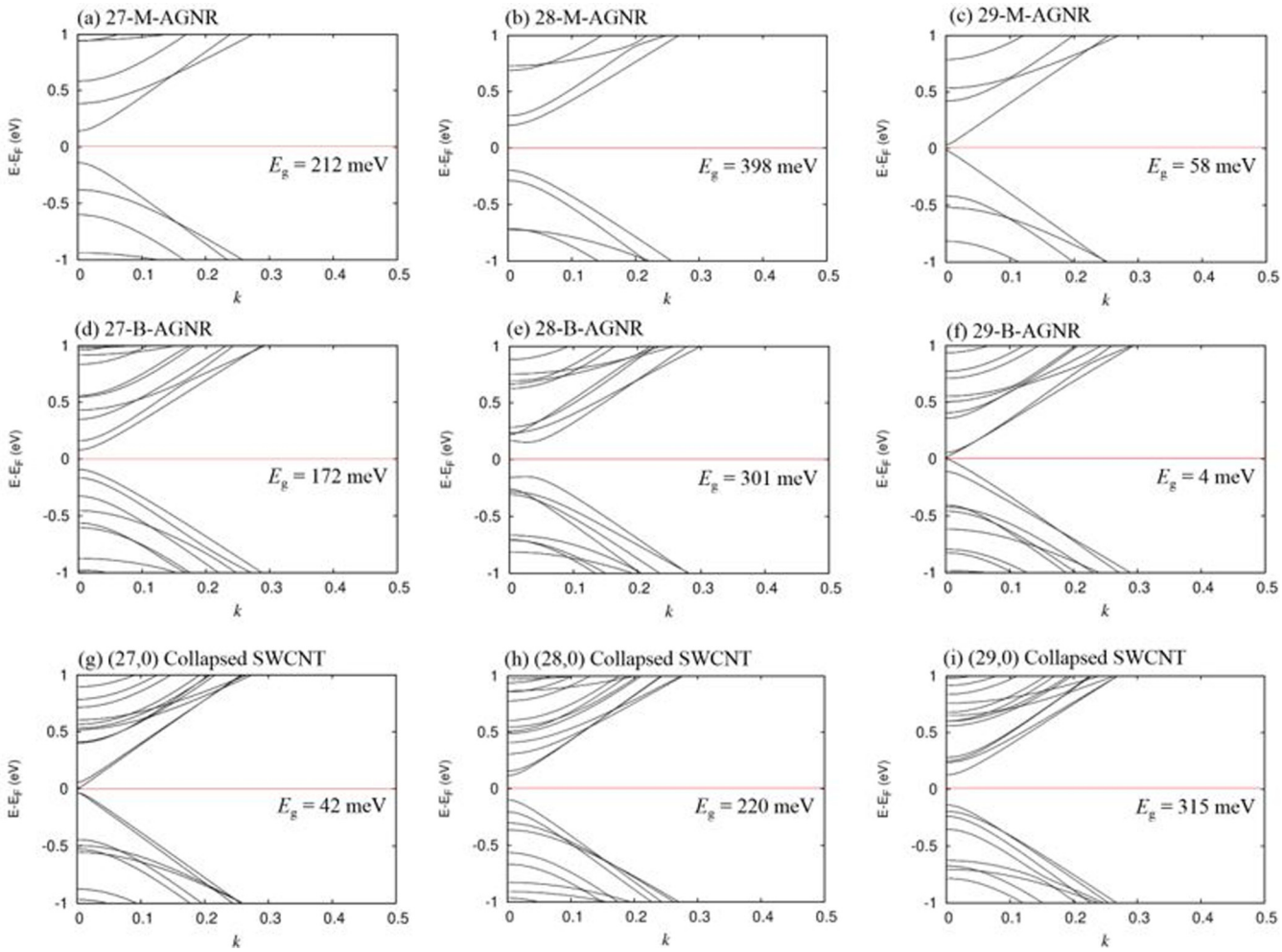

FIG. 17. Sequence of spin-averaged electronic band structures of monolayer (first row), bilayer (second row), AGNRs and collapsed zigzag nanotubes (third row), with number of dimer lines (or chiral index) $N(n) = 27$ (left column), 28 (central column), 29 (right column).

[1] S. Iijima, Nature (London) **354**, 56 (1991).
[2] N. G. Chopra, L. X. Benedict, V. H. Crespi, M. L. Cohen, S. G. Louie, and A. Zettl, Nature (London) **377**, 135 (1995).
[3] T. Hertel, R. E. Walkup, and P. Avouris, Phys. Rev. B **58**, 13870 (1998).
[4] J. Tersoff and R. S. Ruoff, Phys. Rev. Lett. **73**, 676 (1994).
[5] M.-F. Yu, O. Lourie, M. J. Dyer, K. Moloni, T. F. Kelly, and R. S. Ruoff, Science **287**, 637 (2000).
[6] B. I. Yakobson, M. P. Campbell, C. J. Brabec, and J. Bernholc, Comput. Mater. Sci. **8**, 341 (1997).
[7] J. A. Elliott, J. K. W. Sandler, A. H. Windle, R. J. Young, and M. S. P. Shaffer, Phys. Rev. Lett. **92**, 095501 (2004).
[8] M. Terrones, ACS Nano **4**, 1775 (2010).
[9] L. Jiao, X. Wang, G. Diankov, H. Wang, and H. Dai, Nat. Nanotechnol. **5**, 321 (2010).
[10] D. H. Choi, Q. Wang, Y. Azuma, Y. Majima, J. H. Warner, Y. Miyata, H. Shinohara, and R. Kitaura, Sci. Rep. **3**, 1617 (2013).
[11] C.-H. Kiang, J. Phys. Chem. A **104**, 2454 (2000).
[12] S. Lebedkin, P. Schweiss, B. Renker, S. Malik, F. Hennrich, M. Neumaier, C. Stoermer, and M. M. Kappes, Carbon **40**, 417 (2002).
[13] B. Yu, C. Liu, P.-X. Hou, Y. Tian, S. Li, B. Liu, F. Li, E. I. Kauppinen, and H.-M. Cheng, J. Am. Chem. Soc. **133**, 5232 (2011).
[14] L. Ci, R. Vajtai, and P. M. Ajayan, J. Phys. Chem. C **111**, 9077 (2007).
[15] W. Qian, F. Wei, T. Liu, Z. Wang, and Y. Li, J. Chem. Phys. **118**, 878 (2003).
[16] C. Zhang, K. Bets, S. S. Lee, Z. Sun, F. Mirri, V. L. Colvin, B. I. Yakobson, J. M. Tour, and R. H. Hauge, ACS Nano **6**, 6023 (2012).
[17] M. He, J. Dong, K. Zhang, F. Ding, H. Jiang, A. Loiseau, J. Lehtonen, and E. I. Kauppinen, ACS Nano **8**, 9657 (2014).
[18] S. Liu, J. Yue, and R. J. Wehmschulte, Nano Lett.**2**, 1439 (2002).
[19] T. C. Chang and Z. R. Guo, Nano Lett. **10**, 3490 (2010).
[20] N. G. Chopra, F. M. Ross, and A. Zettl, Chem. Phys. Lett. **256**, 241 (1996).
[21] C.-H. Kiang, W. A. Goddard, R. Beyers, and D. S. Bethune, J. Phys. Chem. **100**, 3749 (1996).
[22] V. H. Crespi, N. G. Chopra, M. L. Cohen, A. Zettl, and S. G. Louie, Phys. Rev. B Condens. Matter **54**, 5927 (1996).

[23] V. H. Crespi, N. G. Chopra, M. L. Cohen, A. Zettl, and V. Radmilovic, Appl. Phys. Lett. **73**, 2435 (1998).

[24] R. S. Ruoff, J. Tersoff, D. C. Lorents, S. Subramoney, and B. Chan, Nature (London) **364**, 514 (1993).

[25] X. Yang, G. Wu, J. Zhou, and J. Dong, Phys. Rev. B **73**, 235403 (2006).

[26] X. H. Zhong, R. Wang, L. B. Liu, M. Kang, Y. Y. Wen, F. Hou, J. M. Feng, and Y. L. Li, Nanotechnology **23**, 505712 (2012).

[27] A. C. Torres-Dias, T. F. T. Cerqueira, W. Cui, M. A. L. Marques, S. Botti, D. Machon, M. H. Hartmann, Y. Sun, D. J. Dunstan, and A. San-Miguel, Carbon **123**, 145 (2017).

[28] M. Motta, A. Moisala, I. A. Kinloch, and A. H. Windle, Adv. Mater. **19**, 3721 (2007).

[29] L. X. Benedict, V. H. Crespi, N. G. Chopra, A. Zettl, M. L. Cohen, and S. G. Louie, Chem. Phys. Lett. **286**, 490 (1998).

[30] G. Gao, T. Çagin, and W. A. Goddard III, Nanotechnology **9**, 184 (1998).

[31] H. J. Liu and K. Cho, Appl. Phys. Lett. **85**, 807 (2004).

[32] T. Tang, A. Jagota, C.-Y. Hui, and N. Glassmaker, J. Appl. Phys. **97**, 074310 (2005).

[33] S. Zhang, R. Khare, T. Belytschko, K. J. Hsia, S. L. Mielke, and G. C. Schatz, Phys. Rev. B **73**, 075423 (2006).

[34] M. Hasegawa and K. Nishidate, Phys. Rev. B **74**, 115401 (2006).

[35] J. Xiao, B. Liu, Y. Huang, J. Zuo, K.-C. Hwang, and M.-F. Yu, Nanotechnology **18**, 395703 (2007).

[36] W. Lu, T.-W. Chou, and B.-S. Kim, Phys. Rev. B **83**, 134113 (2011); **84**, 059901(E) (2011).

[37] J. Liu, Arch. Appl. Mech. **82**, 767 (2012).

[38] M. Hasegawa, K. Nishidate, and N. Yoshimoto, Phys. Rev. B **92**, 245429 (2015).

[39] X. Meng, B. Zhang, H. Li, F. Li, Z. Kang, M. Li, and Y. Chen, Int. J. Solids Struct. **160**, 51 (2019).

[40] M. He, J. Dong, H. Wang, H. Xue, Q. Wu, B. Xin, W. Gao, X. He, J. Yu, H. Sun, F. Ding, and J. Zhang, Small **15**, 1804473 (2019).

[41] P. Avouris, M. Freitag, and V. Perebeinos, Nat. Photon. **2**, 341 (2008).

[42] K. Tsukagoshi, N. Yoneya, S. Uryu, Y. Aoyagi, A. Kanda, Y. Ootuka, and B. W. Alphenaar, Phys. B: Condens. Matter **323**, 107 (2002).

[43] F. Kuemmeth, H. O. H. Churcill, P. K. Herring, and C. M. Marcus, Mater. Today **13**, 18 (2010).

[44] S. J. Stuart, A. B. Tutein, and J. A. Harrison, J. Chem. Phys. **112**, 6472 (2000).

[45] S. Plimpton, J. Comput. Phys. **117**, 1 (1995).

[46] M. J. Rayson and P. R. Briddon, Comput. Phys. Commun. **178**, 128 (2008).

[47] M. J. Rayson and P. R. Briddon, Phys. Rev. B **80**, 205104 (2009).

[48] P. R. Briddon and M. J. Rayson, Phys. Status Solidi B **248**, 1309 (2011).

[49] J. P. Perdew, K. Burke, and M. Ernzerhof, Phys. Rev. Lett. **77**, 3865 (1996).

[50] S. Grimme, J. Comput. Chem. **25**, 1463 (2004).

[51] S. Grimme, J. Comput. Chem. **27**, 1787 (2006).

[52] S. Grimme, J. Antony, S. Ehrlich, and H. Krieg, J. Chem. Phys. **132**, 154104 (2010).

[53] S. Grimme, S. Ehrlich, and L. Goergik, J. Comput. Chem. **32**, 1456 (2011).

[54] C. Hartwigsen, S. Goedecker, and J. Hütter, Phys. Rev. B **58**, 3641 (1998).

[55] J. P. Goss, M. J. Shaw, and P. R. Briddon, in *Theory of Defects in Semiconductors*, edited by D. A. Drabold and S. K. Estreicher, Topics in Applied Physics Vol. 104 (Springer, Berlin, Heidelberg, 2007), pp. 69–94.

[56] D. Sheppard, R. Terrell, and G. Henkelmen, J. Chem. Phys. **128**, 134106 (2008).

[57] R. S. Mulliken, J. Chem. Phys. **23**, 2343 (1955).

[58] R. F. Bader, Chem. Rev. **91**, 893 (1991).

[59] A. V. Rozhkov, A. O. Sboychakov, A. L. Rakmanov, and F. Nori, Phys. Rep. **648**, 1 (2016).

[60] Q. Wang, R. Kitaura, Y. Yamamoto, S. Arai, and H. Shinohara, Nano Res. **7**, 1843 (2014).

[61] H. R. Barzegar, E. G.-Espino, A. Yan, C. Ojeda-Aristizabal, G. Dunn, T. Wagberg, and A. Zettl, Nano Lett. **15**, 829 (2015).

[62] R. Zacharia, H. Ulbricht, and T. Hertel, Phys. Rev. B **69**, 155406 (2004).

[63] I. V. Lebedeva, A. V. Lebedev, A. M. Popov, and A. A. Knizhinik, Comput. Mat. Sc. **128**, 45 (2016).

[64] X. Chen, F. Tian, C. Persson, W. Duan, and N.-x. Chen, Sci. Rep. **3**, 3046 (2013).

[65] H. W. Kroto, J. R. Health, S. C. O'Brien, R. F. Curl, and R. E. Smalley, Nature (London) **318**, 162 (1985).

[66] K. Kim, Z. Lee, B. D. Malone, K. T. Chan, B. Alemán, W. Regan, W. Gannett, M. F. Crommie, M. L. Cohen, and A. Zettl, Phys. Rev. B **83**, 245433 (2011).

[67] E. Mostaani, N. D. Drummond, and V. I. Fal'ko, Phys. Rev. Lett. **115**, 115501 (2015).

[68] L. Spanu, S. Sorella, and G. Galli, Phys. Rev. Lett. **103**, 196401 (2009).

[69] H. Shin, J. Kim, H. Lee, O. Heinonen, A. Benali, and Y. Kwon, J. Chem. Theory Comput. **13**, 5639 (2017).

[70] M. Hasegawa and K. Nishidate, e-J. Surf. Sci. Nanotech. **7**, 541 (2009).

[71] J.-Q. Lu, J. Wu, W. Duan, F. Liu, B.-F. Zhu, and B.-L. Gu, Phys. Rev. Lett. **90**, 156601 (2003).

[72] C. E. Giusca, Y. Tison, and S. R. P. Silva, Nano Lett. **8**, 3350 (2008).

[73] H. Mehrez, A. Svizhenko, M. P. Anantram, M. Elstner, and T. Frauenheim, Phys. Rev. B **71**, 155421 (2005).

[74] W.-J. Yin, Y.-E. Xie, L.-M. Liu, Y.-P. Chen, R.-Z. Wang, X.-L. Wei, J.-X. Zhong, and L. Lau, J. Appl. Phys. **113**, 173506 (2013).

[75] M. P. Lima, A. Fazzio, and A. J. R. da Silva, Phys. Rev. B **79**, 153401 (2009).

[76] Y.-W. Son, M. L. Cohen, and S. G. Louie, Nature (London) **444**, 347 (2006).

[77] C.-J. Park, Y.-H. Kim, and K. J. Chang, Phys. Rev. B **60**, 10656 (1999).

[78] T. Nakanishi and T. Ando, Phys. Rev. B **91**, 155420 (2015).

[79] T. Nakanishi and T. Ando, Phys. Rev. B **94**, 155401 (2016).

[80] E. V. Castro, K. S. Novoselov, S. V. Morozov, N. M. R. Peres, J. M. B. L. dos Santos, J. Nilsson, F. Guinea, A. K. Geim, and A. H. Castro Neto, Phys. Rev. Lett. **99**, 216802 (2007).

[81] X. Chen, L. Zhang, Y. Zhao, X. Wang, and C. Ke, J. Appl. Phys. **116**, 164301 (2014).
[82] X. Yuan and Y. Wang, Nanotechnology **29**, 075705 (2018).
[83] C. E. Giusca, Y. Tison, and S. R. Silva, Phys. Rev. B **76**, 035429 (2007).
[84] C. Gómez-Navarro, J. J. Sáenz, and J. Gómez-Herrero, Phys. Rev. Lett. **96**, 076803 (2006).
[85] C. Tao, L. Jiao, O. V. Yazyev, Y.-C. Chen, J. Feng, X. Zhang, R. B. Capaz, J. M. Tour, A. Zettl, S. G. Louie, H. Dai, and M. F. Crommie, Nat. Phys. **7**, 616 (2011).
[86] K. Nishidate and M. Hasegawa, Phys. Rev. B **81**, 125414 (2010).
[87] L. G. Bulusheva, A. V. Okotrub, D. A. Romanov, and D. Tomanek, J. Phys. Chem. A **102**, 975 (1998).
[88] Y.-W. Son, M. L. Cohen, and S. G. Louie, Phys. Rev. Lett. **97**, 216803 (2006).
[89] K.-T. Lam and G. Liang, Appl. Phys. Lett. **92**, 223106 (2008).
[90] V. Barone, O. Hod, and G. E. Scuseria, Nano Lett. **6**, 2748 (2006).
[91] M. Boldoni, A. Sgamellotti, and F. Mercuri, Chem. Phys. Lett. **464**, 202 (2008).
[92] Y. Matsuda, J. Tahir-Kheli, and W. A. Goddard III, J. Phys. Chem. Lett. **1**, 2946 (2010).
[93] L. Yang, C. H. Park, Y. W. Son, M. L. Cohen, and S. G. Louie, Phys. Rev. Lett. **99**, 186801 (2007).
[94] X. Li, X. Wang, L. Zhang, S. Lee, and H. Dai, Science **319**, 1229 (2008).